Phase-Coherent Charge Transport through a Porphyrin Nanoribbon-Graphene Junction

Zhixin Chen[1*†], Jie-Ren Deng[2†], Songjun Hou[3], Xinya Bian[1], Jacob L. Swett[1], Qingqing Wu[3], Jonathan Baugh[4], G. Andrew D. Briggs[1], Jan A. Mol[5], Colin J. Lambert[3*], Harry L. Anderson[2*], and James O. Thomas[1*]

[1]Department of Materials, University of Oxford, Parks Road, Oxford, OX1 3PH, UK

[2]Department of Chemistry, University of Oxford, Chemistry Research Laboratory, Oxford, OX1 3TA, UK

[3]Department of Physics, Lancaster University, Lancaster, LA1 4YB, UK

[4]Institute for Quantum Computing, University of Waterloo, Waterloo, ON N2L 3G1, Canada

[5]School of Physical and Chemical Sciences, Queen Mary University, London, E1 4NS, UK

*zhixin.chen@materials.ox.ac.uk,   *c.lambert@lancaster.ac.uk,   *harry.anderson@chem.ox.ac.uk,
*james.thomas@materials.ox.ac.uk   [†] These authors made equal contributions.

Quantum interference in molecular-scale electronic devices has the potential be exploited in reduced-energy computing and efficient thermoelectric energy harvesting. However, to realise such ambitious goals, it is necessary to demonstrate phase-coherent molecular transport, and to study the hierarchy of quantum interference phenomena that are possible within a given junction. Through the study of a unimolecular device embedded within an electronic graphene Fabry-Pérot interferometer, we show transport is phase-coherent through an 8-nm long porphyrin octamer nanoribbon. Furthermore, we show that interference between molecular and graphene transport pathways results in Kondo and phase-tuneable Fano resonances. The ability to switch between these different transport regimes, and between phase-coherent and sequential tunnelling, opens up strategies for understanding and exploiting interference in molecular-scale electronics and quantum information processing.

The ability to harness and exploit coherence at the nanoscale is crucial for emerging quantum technologies in research areas across engineering, chemistry, and condensed-matter physics.[1] Single-molecule devices are an excellent platform in which to study quantum-coherent phenomena because molecular structures are atomically defined.[2] Recently, bottom-up synthesised graphene[3] and molecular nanoribbons[4] have attracted considerable interest in quantum information processing due to their low dimensionality and associated topological states. Much work in the field of single-molecule junctions has focussed on observing quantum interference (QI) in two-terminal devices by comparing transport properties of homologous series of molecules,[5,6] rather than manipulating QI and phase-coherent transport within the same molecule. From a fundamental viewpoint, the ability to control interference within a given molecule, by tuning between resonant and off-resonant transport is expected to provide new insight into the phase-coherent nature of electrons as they pass through a device. A physical understanding of the signatures of phase-coherent transport, and how transport regimes can be manipulated, is crucial to realise new designs exploiting QI such high-performance single-molecule transistors and efficient thermoelectric generators,[7] as well as for the integration of nanoribbons into solid-state devices.

Molecular devices that use graphene as an electrode material are an ideal platform for investigating phase-coherent phenomena in charge transport,[8-10] because the spatial confinement and long coherence lengths of electrons in graphene mean that devices display resolvable quantum-coherent features, such as electronic Fabry-Pérot interferometry.[11,12] Furthermore, there are established routes to interface molecules with graphene through π-stacking interactions[13] to generate single-molecule graphene junctions with an electrostatic gate, enabling

temperature and magnetic field dependent measurements, with a high operating frequency.[7,14] This is facilitated by the weaker screening of the gate electric field by graphene compared with bulky 3D metallic electrodes used in traditional molecular junctions[15,16] and by its electronic band structure, which makes it possible to differentiate the contributions of graphene and molecular states to transport.[17]

In this work, we study charge transport through porphyrin nanoribbons in graphene-based, three-terminal devices at cryogenic temperatures (Fig. 1a) and demonstrate that conductance measurements as a function of (source-drain) bias voltage (V_{sd}), gate voltage (V_g), magnetic field, and temperature exhibit a wide range of QI phenomena in a single molecule. Our results demonstrate that an 8-nm porphyrin octamer nanoribbon sustains phase-coherent electron transmission that can be tuned electrostatically, and demonstrates a comprehensive picture of the different quantum-coherent phenomena that arise in molecule-graphene junctions.
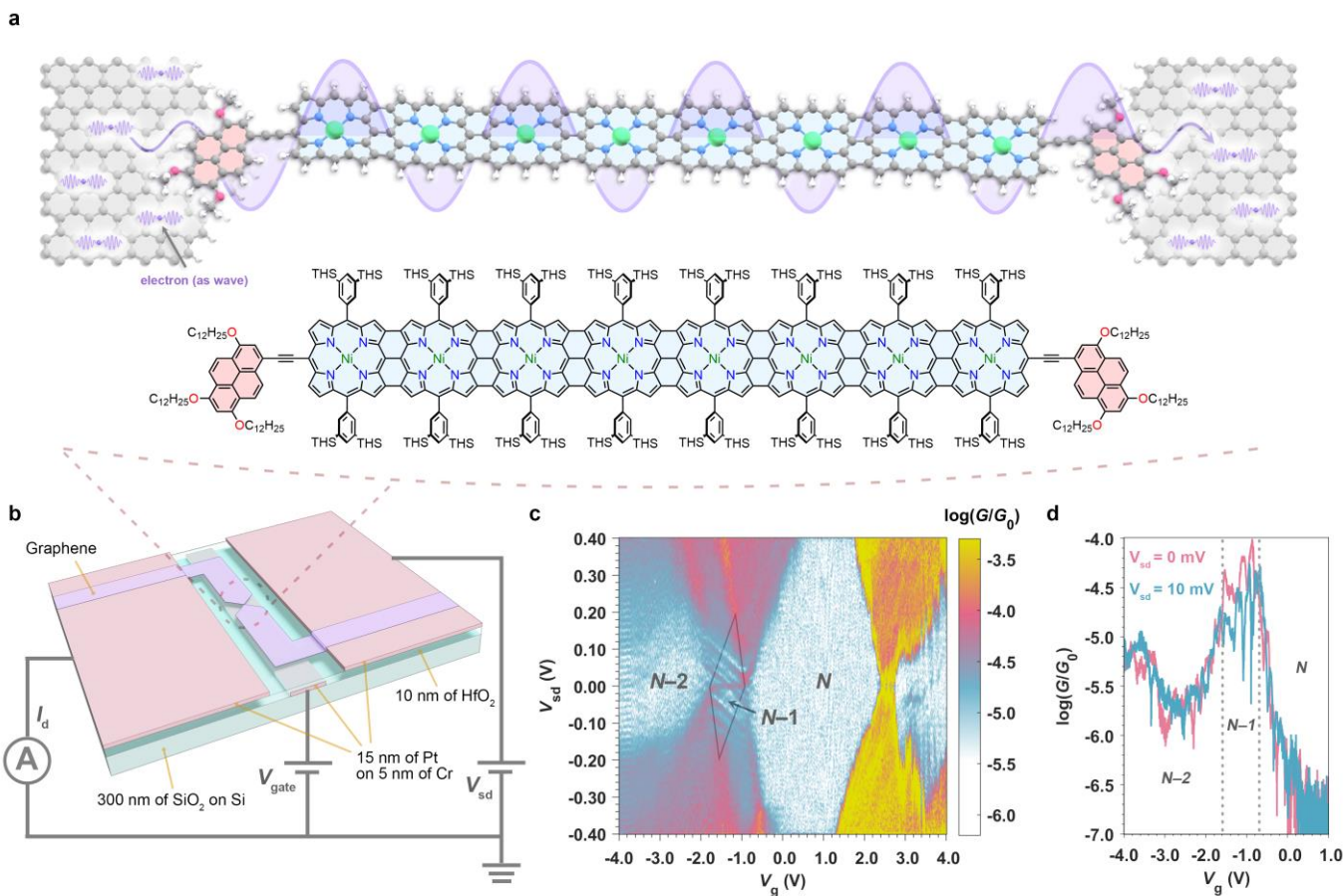
Fig. 1 | Phase-coherent electron transport through a porphyrin nanoribbon-graphene junction. a Schematic representation of phase-coherent electron transport through a graphene-**Ni-FP8** porphyrin nanoribbon-graphene junction (top) and full chemical structure of **Ni-FP8** (bottom). In top panel, solubilising groups on porphyrins (3,5-*bis*(trihexylsilyl)phenyl) and pyrenyls (dodecyloxy) have been omitted for clarity. The purple shaded line indicates the HOMO of the nanoribbon. **b** Device architecture with electronic circuit. The rectangular area in the middle represents the local platinum gate electrode under a 10 nm layer of HfO₂ (transparent light blue); the rectangular areas (pink) at both ends represent the source and drain platinum electrodes, which are in contact with the bowtie-shape graphene (purple). **c** Differential conductance ($G = dI_{sd}/dV_{sd}$) map measured as a function of bias voltage (V_{sd}) and gate voltage (V_g) and **d** differential conductance as a function of V_g at V_{sd} = 0 mV (pink curve) and V_{sd} = 10 mV (blue curve) for **Ni-FP8** device at 4.2 K. The conductance is plotted in logarithmic scale as the ratio to conductance quantum $G_0 = 2e^2/h$ where e is the elementary charge and h is the Planck constant. The N–1 charge state is highlighted by a grey diamond.

Fabrication of single porphyrin-nanoribbon//graphene junctions

We focus on transport in an edge-fused nickel(II) porphyrin octamer (**Ni-FP8**) device (Fig. 1a). **Ni-FP8** has a length

of 8 nm, and we term it a porphyrin nanoribbon, because it has a similar aspect ratio and electronic structure to a graphene nanoribbon.[18,19] The synthesis of the **Ni-FP8** nanoribbon is described in Methods Section, Fig. 1 in Extended Data and Section 2 in Supplementary Information. Most previous transport studies with porphyrin oligomers have used zinc(II) complexes,[20,21] but in this case nickel was used to facilitated the synthesis and to reduce the energy of the HOMO, thus enhancing the chemical stability of the ribbon. The fused porphyrin octamer core is functionalised with pyrene anchor groups to bind to the graphene source and drain electrodes via π-stacking.

A schematic of the device used in this study is shown in Fig. 1b. The architecture comprises nanometre-spaced graphene source and drain electrodes and a platinum electrostatic gate electrode. The gate, covered with a 10 nm HfO_2 dielectric layer, tunes the chemical potentials of the molecular states and the graphene. The device design allows multiple molecular charge states to be measured due to a strong electrostatic coupling between the gate voltage and the molecular states (the gate coupling, α_g, is typically larger than 0.1 eV/V), and the high dielectric breakdown voltage of $V_g \approx \pm 5$ V. We have optimised a previous fabrication procedure to use a Z-shaped pattern for the graphene to reduce tension in the constriction, and use a positive, rather than negative, photoresist to reduce contamination (details of this are given in the Methods section). A combination of these two changes could result in the stronger electronic coupling we observe in this work compared to previous studies.[13] Although we discuss transport through the **Ni-FP8** device in detail, we also present data from shorter porphyrin oligomers in Extended Data Fig. 2: one with zinc porphyrin monomer (**Zn-P1**), one with edge-fused porphyrin trimer (**Zn-FP3**).

Charge transport measurement

The full differential conductance map ($G_{sd} = dI_{sd}/dV_{sd}$) of the porphyrin nanoribbon device, measured at 4.2 K, displays several Coulomb diamonds and associated sequential tunnelling regions (Fig. 1c). We assign the diamond at $V_g = 0$ as the N state (N being the number of electrons on the molecule when it is neutral), as this diamond has a large addition energy, at $E_{add} = 0.7$ eV, that broadly matches the optical HOMO-LUMO gap (energy of the longest wavelength absorption band; 1750 nm, 0.71 eV). There is a zero-bias conductance peak in the smaller neighbouring diamond between $V_g \sim -0.7$ V and $V_g \sim -1.4$ V, which is a Kondo resonance (discussed in detail below) that results from screening of an unpaired spin on the nanoribbon by electrons within the graphene electrodes.[22,23] The observation of a Kondo resonance is consistent with assigning this smaller diamond to the odd $N-1$ (i.e. **Ni-FP8⁺**) state, and the larger diamond at $V_g = 0$ to the N state, because N is even for **Ni-FP8** and the number of electrons on the molecule differs by one between adjacent Coulomb diamonds.[24] The two sequential transport regions with broad edges which flank the $N-1$ diamond are then the $N-1/N$ charge transition ($V_g \sim -0.7$ V) and $N-2/N-1$ transition ($V_g \sim -1.4$ V). Finally, the highly conductive region at positive V_g is the $N/N+1$ charge transition. We calculate the coupling of the molecular levels to the gate and source potentials from the slopes of the Coulomb diamonds, as $\alpha_g = 0.22$ eV/V, and $\alpha_s = 0.65$ eV/V respectively, giving the fraction of each applied potential that shift the molecular levels.[16]

Considering the low measurement temperature (4.2 K, $k_BT = 0.4$ meV), the poor definition in the boundaries of the Coulomb diamonds (FWHM of Coulomb peaks ~ 6 meV) is attributed to lifetime broadening that results from intermediate molecule-electrode coupling, consistent with appearance of the Kondo resonance.[25,26] The broad diamonds suggests there are large regions where the molecular charge state is not well defined, in contrast with a device in the weakly coupled regime (commonly observed for molecules π-stacked to graphene electrodes[13,16,27]), where conductance occurs only within the sequential transport regions (when the chemical potentials of molecular transitions lie within the bias window, neglecting coherent resonant tunnelling) separated by Coulomb diamonds. In Fig. 1c and 1d we clearly observe off-resonance transport features that even at $V_{sd} = 10$ mV (away from the Kondo peak) show that the conductance is not completely suppressed, instead remaining above the noise except

within the *N* diamond, indicating significant contributions from phase-coherent transport around the *N*–1/*N* and *N*–2/*N*–1 transitions of the intermediately coupled nanoribbon device.[25] As the hybridisation between molecule and electrode increases with electronic coupling, the transport through the molecular junction can only be fully understood by considering the entire graphene-nanoribbon-graphene system. We discuss the mixture of effects that arise from this holistic approach in the next three sections with the following order: first, we discuss phase-coherent transport interference *within* the graphene channel, secondly interference *between* graphene states and molecular states, and thirdly, we discuss off-resonant molecular transport.
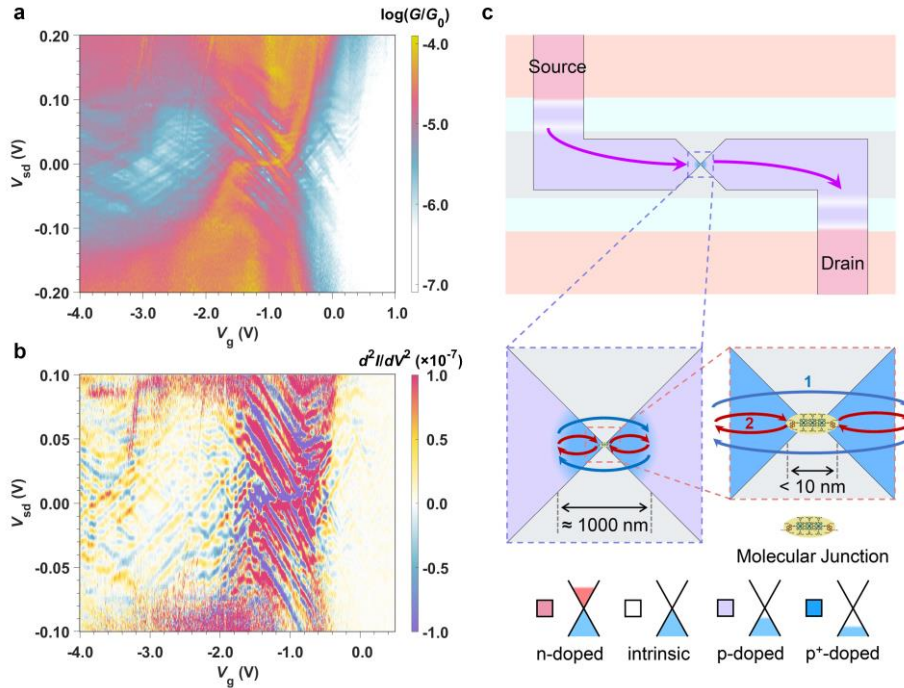

Fig. 2 | Fabry-Pérot interference. a Detailed conductance map of the interference pattern overlapping with molecular charge transitions. **b** Derivative of differential conductance (dI^2_d/dV^2_{sd}) measured as a function of bias voltage (V_{sd}) and gate voltage (V_g). **c** Schematic of possible interference conditions. Two possible resonance conditions for Fabry-Pérot interference are indicated by arrows within the highly doped region (blue) and on the molecule-graphene interfaces (red). The trajectories are within the graphene, although they are shown to extend outside for clarity.

Graphene-based interference

A high-resolution conductance map of the *N*–2/*N*–1 and *N*–1/*N* transitions is shown in Fig. 2a. There is periodic structure within the off-resonant conductance, especially in the range ± 100 mV, with a weaker electrostatic coupling to the gate ($\alpha_g = 0.05$ eV/V) than the molecular states. The effect is more obvious in the second derivative of the current (dI^2_{sd}/dV^2_{sd}) map which displays a 'chequerboard' pattern (Fig. 2b).

We explore the origins of the 'chequerboard' pattern by plotting a two-dimensional fast Fourier transform (FFT) of the dI^2_{sd}/dV^2_{sd} map (Fig. S4-1). Hot spots in the FFT show the smallest energy spacings in the conductance maps correspond to about 5 and 10 meV. Similar periodicity has been observed in transport measurements in graphene and is attributed to the formation of an electronic Fabry-Pérot (FP) interferometer within the graphene channel.[11,12,28] By analogy with an optical FP cavity formed from a pair of partially reflective mirrors; two potential steps, induced by doping, define an electronic FP cavity. Considering resonances within a one-dimensional FP cavity, our measured periodic energy spacings of 5 and 10 meV correspond to cavity lengths of $L = hv_F/(2E) =$ 1000 nm and 500 nm, using the Fermi velocity of $v_F = 2.4 \times 10^6$ m/s for CVD graphene.[28] These length scales are an order of magnitude larger than those associated with reflections within the **Ni-FP8** nanoribbon itself, indicating the QI pattern is dominated by reflections within the graphene channel, which is further verified by

4

magnetoconductance oscillations shown in Extended Data Fig. 3.

The cavity is formed within graphene by doping induced by the substrate. Graphene transferred onto HfO_2 is *p*-doped (light purple area),[29] shown schematically in Fig. 2c. The electroburning process that is used to create the nanogap anneals the graphene and increases the hole concentration local to the tunnel junction, generating a highly doped (p^+-doped) region (blue area) of ~ 1000 nm in diameter.[28] Therefore reflections over 500 nm occur between a pp^+ potential step and a molecule/electrode tunnel barrier, as highlighted by red arrows in Fig. 2c. As the length of the molecule is much shorter than the graphene cavity, reflections from either sides of the molecule-graphene interface are not distinguishable. For the reflections with a 1000 nm cavity (the diameter of the p^+-doped region) the interfaces between *p*-doped and p^+-doped graphene regions generate the potential steps, the electrons are reflected or transmitted within the pp^+p cavity that contains the molecular junction, as indicated by blues arrows in Fig 2c. This is the first experimental demonstration of quantum interference within a FP cavity that contains a molecular junction at the centre, and demonstrates that electron transmission through the molecule is phase coherent.
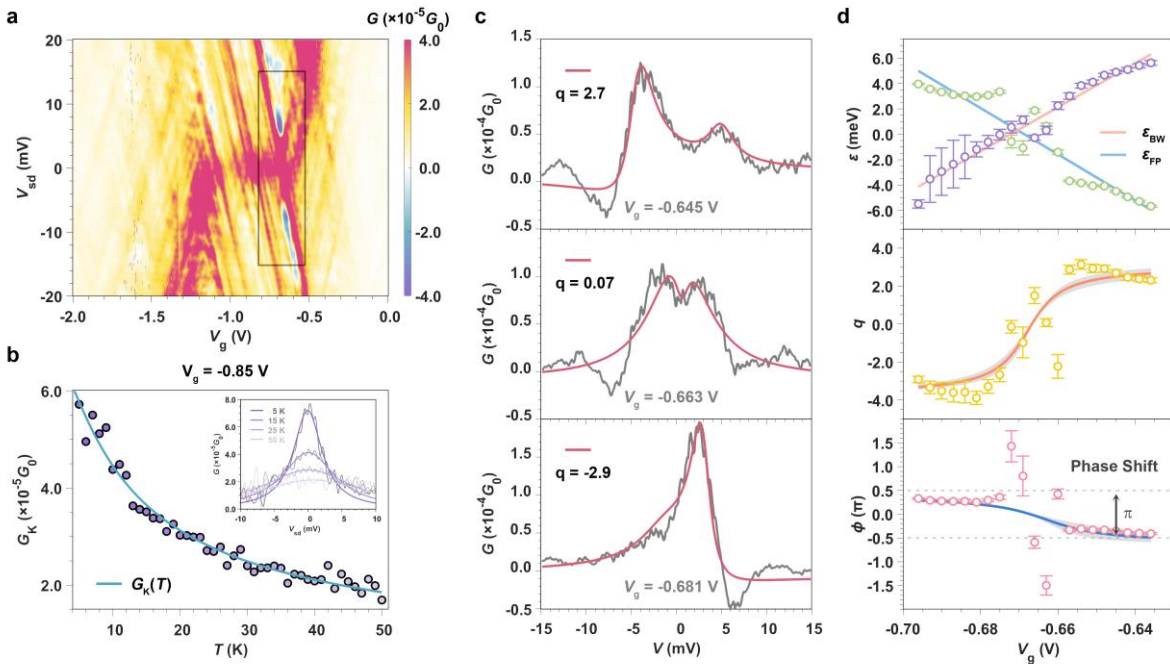

Fig. 3 | Kondo and Fano resonances. a Detailed differential conductance map of the region with Kondo resonance. The overlapping interference pattern and Kondo resonance results in a fluctuating zero-bias enhancement. **b** Example for fitting (blue line) of Kondo temperature measured at V_g = −0.85 V. The purple dots indicate experimental differential conductance of the Kondo peak ($G_K(T)$). Inset: experimental differential conductance as a function of bias voltage (V_{sd}) (grey curves) and the Lorentzian fittings of Kondo peaks (purple curves). Colours from dark to light indicate lower to higher temperature. **c** Conductance traces (grey) and fits (red) for when $\varepsilon_{FP} > \varepsilon_{BW}$ (top) $\varepsilon_{FP} \sim \varepsilon_{BW}$ (middle) and $\varepsilon_{FP} < \varepsilon_{BW}$ (bottom). **d** The fitted energy of the molecular level Breit-Wigner (BW) resonance for (ε_{BW}, purple) and energy of the graphene Fabry-Pérot (FP) resonance (ε_{FP}, green) from Fano fits, and their linear response (pink line for ε_{BW}, light blue line for ε_{FP}) to gate potentials (top panel), and the values of the fitted Fano asymmetry parameter, q (middle panel). The phase shift between the two transport channels is related to q through: $\phi = \arctan - q^{-1}$, and the experimental values of phase (pink dots) show a π shift upon scanning through −0.663 V. The blue line is a fit to: $\phi = -\arctan\left[k(V_g - V_c)\right]$, with V_c = −0.663 V, k^{-1}= 6 meV (bottom panel).

Interference between graphene and molecular states

As shown in Fig. 2a, the effects of coherent transmission within the graphene channel appear alongside transport features (i.e. Coulomb blockade and associated sequential transport) of the **Ni-FP8** nanoribbon, and the interplay of these two transport channels leads to many-body interference effects. First, we consider the FP and Kondo resonances. Fig. 3a displays a high-resolution scan in the region of the N–$2/N$–1 and N–$1/N$ charge state transitions, displaying the zero-bias Kondo resonance only within the V_g range of the N–1 charge state (when the nanoribbon is oxidised to S = 1/2 **Ni-FP8$^+$**). A typical gate-dependent measurement of a Kondo resonance would give a Kondo valley described by the Haldane relation, i.e., a zero-bias conductance peak and associated Kondo temperature, T_K, that dips between the two charge-state transitions that define the odd charge state.[22,30] However, as a spin-1/2 Kondo resonance is due to transport through a many-body state that results from exchange between the **Ni-FP8$^+$** spin and electrons at the Fermi surface of the leads, T_K also depends exponentially on the graphene density of states.[31] Therefore our gate-dependent measurement of the Kondo peak displays a conductance oscillation within the N–1 state as the FP peaks move in and out of resonance, as opposed to a smooth valley (Fig. 3a, and also pink gate trace in Fig. 1d). We fit the temperature-dependent conductance data to a spin-1/2 Kondo model $G_K(T) = G_{T=0}/\left[1+\left(2^{1/s}-1\right)\left(T/T_K\right)^2\right]^s$ where $G_K(T)$ is the differential conductance at the peak of Kondo resonance, $G_{T=0}$ is the differential conductance of the Kondo peak at zero temperature, and s is an empirical parameter.[30] At V_g = –0.85 V, a voltage with no nearby overlapping peaks, we calculate T_K = 18 ± 1 K and s = 0.30 ± 0.04. We also obtain T_K at this gate voltage from the FWHM of the resonance that gives a similar value of 17 ± 1 K. (see Fig. 3b, inset).[32] Due to the overlap of the FP and Kondo resonances, T_K, as well as conductance, oscillates within the Kondo valley[33] (see Extended Data Fig. 3 for temperature dependence at other V_g).

Next, we address the interference between the FP resonances and the resonant tunnelling pathway through the molecule itself. As described above, the FP resonances and the Coulomb resonances have different gate couplings, meaning the lines of the FP resonances intersect the resonant tunnelling regions at various values of (V_g, V_{sd}). In the region around the N–$1/N$ Coulomb peak where this occurs (Fig. 3a, highlighted box) low-bias conductance traces display Fano line shapes (Fig. 3c). Fano resonances are characteristic of interference between a localised state (molecular orbital) and a quasi-continuous (FP resonance) state. We describe conductance around the Coulomb peak by:

$$G = G_{BW} + G_{bg}\frac{(\tilde{\varepsilon}+q)^2}{\tilde{\varepsilon}^2+1} \qquad\qquad \text{equation (1)}$$

where $\tilde{\varepsilon} = \left(\varepsilon-\varepsilon_{FP}\right)/\left(\Gamma_{Fano}/2\right)$ is the dimensionless reduced detuning, with ε_{FP} the energy of the FP resonance and Γ_{Fano} the coupling between the two channels, and q is the Fano asymmetry parameter. The first term describes the molecular transition as a Breit-Wigner (BW) resonance:[28]

$$G_{BW} = A\frac{\Gamma^2}{\left(\varepsilon-\varepsilon_{BW}\right)^2+\Gamma^2} \qquad\qquad \text{equation (2)}$$

with Γ the molecule-electrode coupling, ε_{BW} the energy of the resonance, and A and G_{bg} are pre-factors. The energy of the two resonances depend linearly on V_g (Fig. 3c), as expected from the conductance map, and the couplings are fitted as Γ = 3.8 ± 2.3 meV and Γ_{Fano} = 2.7 ± 0.5 meV. The two channels cross zero bias at V_g = – 0.663 V, and we measure the corresponding mirrored Fano profiles (Fig. 3c) associated with a change in the sign of q as we transition from $\varepsilon_{FP}>\varepsilon_{BW}$ to $\varepsilon_{FP}<\varepsilon_{BW}$ (Fig. 3d). When the two channels are simultaneously on resonance, we find $q \sim 0$ and observe the expected conductance dip on the BW peak (Fig. 3c, middle). The Fano

asymmetry parameter, q, is the cotangent of the phase shift between the two transport channels,[34] and as V_g is scanned through the Coulomb peak there is a transmission phase shift (ϕ) of π (Fig. 3d), that is either due a transmission zero arising from the Fano resonance or a change in occupancy of the nanoribbon, in accordance the Friedel Sum Rule.[35-37] The evolution of the Fano resonance line shape across the Coulomb peak provides addition evidence that a portion of the molecular resonant transport around the Coulomb peak is phase coherent. Typically it is not possible to measure phase directly in conductance measurements (apart from in specific device architectures in which transmission pathways are spatially separated[38]) as conductance is the absolute square of the transmission amplitude, however our results demonstrate that incorporating a molecular junction within a FP cavity allows the transmission phase shift to be experimentally determined.

Phase-coherent molecular transport

Finally, we describe the molecular transport in more detail, and in particular the temperature and charge-state dependence. We measured conductance up to 80 K, and as the thermal energy increases beyond hv_F/L (5 meV), the FP interference pattern, which is just visible at 40 K (k_BT = 3.5 meV) (Fig. 4a), disappears by 80 K (k_BT = 6.9 meV, comparable to $\Gamma \sim 6$ meV, Fig. 4b). As shown in Fig. 4c, 4d and 4e, the conductance of the Coulomb peaks show a weak temperature dependence. In the regions of V_g between the Coulomb peaks, where off-resonant transport is measured through the molecular junction, the conductance is temperature independent, consistent with off-resonant phase-coherent transport being the dominant mechanism (more temperature-dependent data is in Supplementary Information). This constitutes one of the longest molecular systems (8 nm) with well-defined anchoring over which phase-coherent transport has been measured, resulting from low attenuation factors associated with edge-fused porphyrin oligomers.[39]
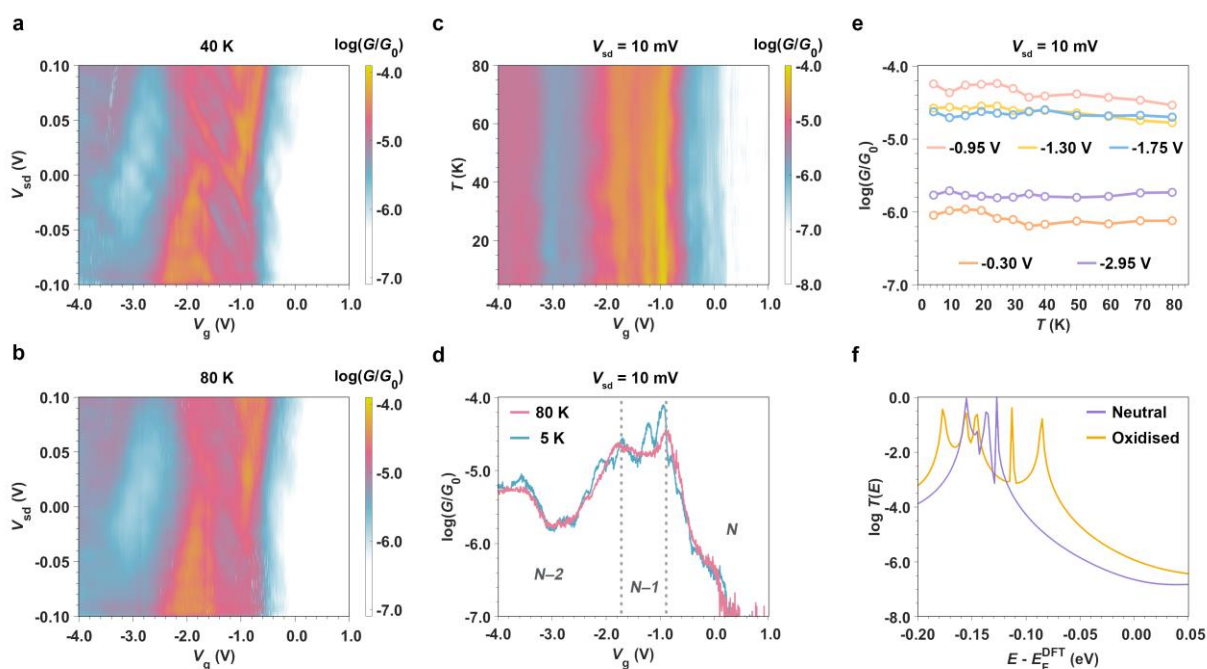

Fig. 4 | Temperature dependence. The fluctuations of conductance from interference disappear as thermal energy surpasses hv_F/L (5 meV) and the coherence length decreases, shown in the conductance maps at **a** 40 K (k_BT = 3.5 meV) and **b** 80 K (6.9 meV). **c** Differential conductance map measured as a function of temperature and gate voltage. Indicative of phase coherent transport, the conductance does not depend obviously on temperature. **d** Differential conductance as a function of V_g measured at 5 K (blue curve) and 80 K (pink curve) with a fixed bias voltage V_{sd} = 10 mV. **e** Temperature dependence of off-resonant transport in N–2 (–2.95 V), N–1 (–1.3 V), and N (–0.3 V) charge states and the N–2/N–1 (–1.75 V) and N–1/N (–0.95 V) Coulomb peaks. Note

there is a shift in the position of the Coulomb peaks from Fig. 2, likely to be a result in a change in trap occupancy in the HfO$_2$. For **a**, **b** and **e** the conductance was measured V_{sd} = 10 mV to exclude the impact of Kondo resonance. **f** Calculated transmission spectra for the neutral state (purple) and oxidised state (orange) of single-molecule junction.

The off-resonance conductance is strongly dependent on the charge state of **Ni-FP8**, with conductance of the neutral nanoribbon (0.5 V_g away from the N–1/N Coulomb peak) just above the noise level of our experimental set-up (10$^{-6.2}$ G$_0$), but around 10$^{-4.6}$ G$_0$ in the N–1 state and 10$^{-5.8}$ G$_0$ in N–2 (0.8 V_g away from the N–2/N–1 Coulomb peak), indicating that in the oxidised states of the **Ni-FP8**, off-resonance coherent transport is more efficient than in the neutral state. Charge-state dependence of conductance has been observed previously in STM-BJ measurements of fused porphyrin oligomers,[40] with a similar conductance enhancement of ~100 for an edge-fused trimer, similar to the ratio measured in our device that has a quite different geometry. Furthermore, our results are consistent with the general observation in single-molecule conductance measurements that upon oxidation or reduction, a conductance enhancement is observed in the odd-electron-number state[41-43]. As with these previous studies, we can utilize a combination of DFT and quantum transport theory[45-47] to calculate the phase-coherent transmission (see the details in Methods Section) to support our experimental observations of a change in off-resonant conductance after **Ni-FP8** oxidation. To model the effect of a gate potential in the calculations, Cl atoms are placed on top of each Ni atom in the fused octamer to enable transmission to be calculated for an oxidised nanoribbon. The transmission coefficient T(E) (orange curve), when eight Cl atoms are present, is plotted in Fig. 4f and for comparison, the transmission coefficient (purple curve) of the neutral octamer is also shown. In agreement with our measurements, upon oxidation, a clear increase in $T(E)$ is observed over a large energy range close to Fermi energy, primarily due to a shrinking of the HOMO-LUMO gap (Fig. S6-2 in Supplementary Information). The introduction of Cl atoms does create extra features (spikes) in the transmission, but these do not affect the increasing trend (see Fig. S6-2 in Supplementary Information). The calculated transmission spectra based on coherent transport theory show excellent agreement with the experimental measurements of **Ni-FP8**, particularly at higher temperature. To demonstrate that our conclusion is resilient to the contact details, we have considered two further anchoring scenarios. In the first new scenario, a pyrene and a porphyrin are attached to the right electrode, while only a pyrene is attached to the left electrode. This breaks the symmetry of the junction. In the second case, a pyrene and a porphyrin are attached to the right electrode, and a pyrene and a porphyrin are attached to the left electrode, which creates a more symmetric junction. As shown by their transmission coefficients in the bottom panel of Fig. S6-4, in both cases, the conductance increases upon oxidation, which demonstrates that this tendency is robust and common a common feature of different anchoring scenarios.

Conclusions

Our results provide a comprehensive account of the interplay between molecule, electrode, and many-body states that constitute transport pathways in a graphene-based single-molecule junction. The different transport channels allow phase shifts in the transmission to be measured around the Coulomb peak within a molecular device for the first time, and demonstrates a route to obtain phase information encoded in molecular orbitals via conductance measurements. The ability to tune a molecule between different transport regimes opens up new strategies for exploiting QI in molecular-scale devices, and demonstrates an important step in the process of integrating molecular nanoribbons into solid-state devices.

Reference

1   Heinrich, A. J. *et al.* Quantum-coherent nanoscience. *Nat. Nanotechnol.* **16**, 1318-1329, doi:10.1038/s41565-021-00994-1 (2021).

2   Su, T. A., Neupane, M., Steigerwald, M. L., Venkataraman, L. & Nuckolls, C. Chemical principles of single-molecule electronics. *Nat. Rev. Mater.* **1**, 16002, doi:10.1038/natrevmats.2016.2 (2016).

3   Groning, O. *et al.* Engineering of robust topological quantum phases in graphene nanoribbons. *Nature* **560**, 209-213, doi:10.1038/s41586-018-0375-9 (2018).

4   Cirera, B. *et al.* Tailoring topological order and pi-conjugation to engineer quasi-metallic polymers. *Nat. Nanotechnol.* **15**, 437-443, doi:10.1038/s41565-020-0668-7 (2020).

5   Xin, N. *et al.* Concepts in the design and engineering of single-molecule electronic devices. *Nat. Rev. Phys.* **1**, 211-230, doi:10.1038/s42254-019-0022-x (2019).

6   Liu, J., Huang, X., Wang, F. & Hong, W. Quantum Interference Effects in Charge Transport through Single-Molecule Junctions: Detection, Manipulation, and Application. *Acc. Chem. Res.* **52**, 151-160, doi:10.1021/acs.accounts.8b00429 (2019).

7   Gehring, P., Thijssen, J. M. & van der Zant, H. S. J. Single-molecule quantum-transport phenomena in break junctions. *Nat. Rev. Phys.* **1**, 381-396, doi:10.1038/s42254-019-0055-1 (2019).

8   Miao, F. *et al.* Phase-coherent transport in graphene quantum billiards. *Science* **317**, 1530-1533, doi:10.1126/science.1144359 (2007).

9   Caneva, S. *et al.* Mechanically controlled quantum interference in graphene break junctions. *Nat. Nanotechnol.* **13**, 1126-1131, doi:10.1038/s41565-018-0258-0 (2018).

10   Berger, C. *et al.* Electronic confinement and coherence in patterned epitaxial graphene. *Science* **312**, 1191-1196, doi:10.1126/science.1125925 (2006).

11   Deprez, C. *et al.* A tunable Fabry-Perot quantum Hall interferometer in graphene. *Nat. Nanotechnol.* **16**, 555-562, doi:10.1038/s41565-021-00847-x (2021).

12   Ronen, Y. *et al.* Aharonov-Bohm effect in graphene-based Fabry-Perot quantum Hall interferometers. *Nat. Nanotechnol.* **16**, 563-569, doi:10.1038/s41565-021-00861-z (2021).

13   Limburg, B. *et al.* Anchor Groups for Graphene-Porphyrin Single-Molecule Transistors. *Adv. Funct. Mater.* **28**, 1803629, doi:10.1002/adfm.201803629 (2018).

14   Zhang, J. *et al.* Single-molecule electron transfer in electrochemical environments. *Chem Rev* **108**, 2737-2791, doi:10.1021/cr068073+ (2008).

15   Jia, C., Ma, B., Xin, N. & Guo, X. Carbon Electrode-Molecule Junctions: A Reliable Platform for Molecular Electronics. *Acc. Chem. Res.* **48**, 2565-2575, doi:10.1021/acs.accounts.5b00133 (2015).

16   Mol, J. A. *et al.* Graphene-porphyrin single-molecule transistors. *Nanoscale* **7**, 13181-13185, doi:10.1039/c5nr03294f (2015).

17   Gehring, P. *et al.* Distinguishing Lead and Molecule States in Graphene-Based Single-Electron Transistors. *ACS Nano* **11**, 5325-5331, doi:10.1021/acsnano.7b00570 (2017).

18   Chen, L., Hernandez, Y., Feng, X. & Mullen, K. From nanographene and graphene nanoribbons to graphene sheets: chemical synthesis. *Angew. Chem. Int. Ed. Engl.* **51**, 7640-7654, doi:10.1002/anie.201201084 (2012).

19   Tsuda, A. & Osuka, A. Fully conjugated porphyrin tapes with electronic absorption bands that reach into infrared. *Science* **293**, 79-82, doi:10.1126/science.1059552 (2001).

20   Sedghi, G. *et al.* Long-range electron tunnelling in oligo-porphyrin molecular wires. *Nat. Nanotechnol.* **6**, 517-523, doi:10.1038/nnano.2011.111 (2011).

21   Zwick, P., Dulic, D., van der Zant, H. S. J. & Mayor, M. Porphyrins as building blocks for single-molecule devices. *Nanoscale* **13**, 15500-15525, doi:10.1039/d1nr04523g (2021).

22   Liang, W., Shores, M. P., Bockrath, M., Long, J. R. & Park, H. Kondo resonance in a single-molecule transistor.

Nature **417**, 725-729, doi:10.1038/nature00790 (2002).

23   Park, J. *et al.* Coulomb blockade and the Kondo effect in single-atom transistors. *Nature* **417**, 722-725, doi:10.1038/nature00791 (2002).

24   Perrin, M. L., Burzuri, E. & van der Zant, H. S. Single-molecule transistors. *Chem. Soc. Rev.* **44**, 902-919, doi:10.1039/c4cs00231h (2015).

25   Moth-Poulsen, K. & Bjornholm, T. Molecular electronics with single molecules in solid-state devices. *Nat. Nanotechnol.* **4**, 551-556, doi:10.1038/nnano.2009.176 (2009).

26   Osorio, E. A., Bjornholm, T., Lehn, J. M., Ruben, M. & van der Zant, H. S. Single-molecule transport in three-terminal devices. *J Phys Condens Matter* **20**, 374121, doi:10.1088/0953-8984/20/37/374121 (2008).

27   Prins, F. *et al.* Room-temperature gating of molecular junctions using few-layer graphene nanogap electrodes. *Nano Lett.* **11**, 4607-4611, doi:10.1021/nl202065x (2011).

28   Gehring, P. *et al.* Quantum Interference in Graphene Nanoconstrictions. *Nano Lett.* **16**, 4210-4216, doi:10.1021/acs.nanolett.6b01104 (2016).

29   Song, S. M. & Cho, B. J. Investigation of interaction between graphene and dielectrics. *Nanotechnology* **21**, 335706, doi:10.1088/0957-4484/21/33/335706 (2010).

30   Scott, G. D. & Natelson, D. Kondo resonances in molecular devices. *ACS Nano* **4**, 3560-3579, doi:10.1021/nn100793s (2010).

31   Hewson, A. C. *The Kondo Problem to Heavy Fermions*.   (Cambridge University Press, 2009).

32   Nagaoka, K., Jamneala, T., Grobis, M. & Crommie, M. F. Temperature Dependence of a Single Kondo Impurity. *Phys. Rev. Lett.* **88**, 077205, doi:10.1103/PhysRevLett.88.077205 (2002).

33   I, V. B. *et al.* Observation of the Kondo screening cloud. *Nature* **579**, 210-213, doi:10.1038/s41586-020-2058-6 (2020).

34   Limonov, M. F., Rybin, M. V., Poddubny, A. N. & Kivshar, Y. S. Fano resonances in photonics. *Nature Photonics* **11**, 543-554, doi:10.1038/Nphoton.2017.142 (2017).

35   Martin, R. M. Fermi-Surfae Sum Rule and its Consequences for Periodic Kondo and Mixed-Valence Systems. *Phys. Rev. Lett.* **48**, 362-365, doi:10.1103/PhysRevLett.48.362 (1982).

36   Takada, S. *et al.* Transmission phase in the Kondo regime revealed in a two-path interferometer. *Phys. Rev. Lett.* **113**, 126601, doi:10.1103/PhysRevLett.113.126601 (2014).

37   Xu, H. Q. & Sheng, W. D. Discontinuity in the phase evolution of electron transport in a quantum channel with attached quantum dots. *Physical Review B* **57**, 11903-11906, doi:DOI 10.1103/PhysRevB.57.11903 (1998).

38   Schuster, R. *et al.* Phase measurement in a quantum dot via a double-slit interference experiment. *Nature* **385**, 417-420, doi:DOI 10.1038/385417a0 (1997).

39   Leary, E. *et al.* Bias-Driven Conductance Increase with Length in Porphyrin Tapes. *J. Am. Chem. Soc.* **140**, 12877-12883, doi:10.1021/jacs.8b06338 (2018).

40   Leary, E. *et al.* Long-lived charged states of single porphyrin-tape junctions under ambient conditions. *Nanoscale Horiz* **6**, 49-58, doi:10.1039/d0nh00415d (2021).

41   O'Driscoll, L. J. *et al.* Electrochemical control of the single molecule conductance of a conjugated bis(pyrrolo)tetrathiafulvalene based molecular switch. *Chem Sci* **8**, 6123-6130, doi:10.1039/c7sc02037f (2017).

42   Liu, J. *et al.* Radical-Enhanced Charge Transport in Single-Molecule Phenothiazine Electrical Junctions. *Angew. Chem. Int. Ed. Engl.* **56**, 13061-13065, doi:10.1002/anie.201707710 (2017).

43   Koole, M., Thijssen, J. M., Valkenier, H., Hummelen, J. C. & van der Zant, H. S. Electric-Field Control of Interfering Transport Pathways in a Single-Molecule Anthraquinone Transistor. *Nano Lett.* **15**, 5569-5573, doi:10.1021/acs.nanolett.5b02188 (2015).

44   Soler, J. M. *et al.* The SIESTA method forab initioorder-Nmaterials simulation. *J. Phys.: Condens. Matter* **14**, 2745-2779, doi:10.1088/0953-8984/14/11/302 (2002).

45   Ferrer, J. *et al.* GOLLUM: a next-generation simulation tool for electron, thermal and spin transport. *New J. Phys.* **16**, 093029, doi:10.1088/1367-2630/16/9/093029 (2014).

46   Lambert, C. J., Physics, I. o. & Publishing, I. o. P. *Quantum Transport in Nanostructures and Molecules: An Introduction to Molecular Electronics.* (IOP Publishing, 2021).

Methods

Synthesis of Ni-FP8. To a solution of **Ni-LP8Br** (2.0 mg, 0.15 µmol, 1 equiv.) in dry 1,2-dichloroethane (DCE, 2.5 mL), a suspension of $AuCl_3$ (0.64 mg, 2.1 µmol, 14 equiv.) and AgOTf (2.7 mg, 11 µmol, 70 equiv.) in dry DCE (2.5 mL) was added dropwise and the reaction mixture was stirred at 25 ºC for 15 min. After that, a suspension of $AuCl_3$ (0.13 mg, 0.42 µmol, 2.8 equiv.) and AgOTf (0.54 mg, 2.1 µmol, 14 equiv.) in dry DCE (0.5 mL) was added dropwise to the reaction mixture and the reaction was monitored by UV-vis-NIR spectroscopy with CH_2Cl_2 + 1% triethylamine as solvent. After the completion, triethylamine (1.0 mL) was added to the reaction mixture. The resulting mixture was purified by flash column chromatography on silica gel using pentane/CH_2Cl_2 (9:1) as eluent to give product **Ni-FP8Br** (1.0 mg, 50% yield).

A mixture of **Ni-FP8Br** (1.0 mg, 0.075 µmol, 1.0 equiv.), Pd(PPh$_3$)$_4$ (1.1 mg, 1.5 µmol, 20 equiv.) and CuI (0.14 mg, 0.75 µmol, 10 equiv.) in dry toluene (0.5 mL) and diisopropylamine (DIPA, 0.5 mL) was degassed by three freeze-pump-thaw cycles. A solution of 1,3,6-tris(dodecyloxy)-8-ethynylpyrene (10 mg, 13 µmol, 170 equiv.) in dry toluene (0.5 mL) and DIPA (0.5 mL) was degassed by three freeze-pump-thaw cycles and transferred to the reaction mixture under argon. After that, the mixture was stirred at 50 ºC under argon for 2 h. Then, a degassed solution of 1,3,6-tris(dodecyloxy)-8-ethynylpyrene (5.0 mg, 6.4 µmol, 85 equiv.) in dry toluene (0.5 mL) and DIPA (0.5 mL) was added to the reaction mixture and the mixture stirred at 50 ºC for another 20 h. After reaction, the resulting mixture was separated by flash column chromatography on silica gel using pentane/CH_2Cl_2 (1:1) as eluent, followed by size-exclusion chromatography (Biorad Bio beads SX-1) with toluene/pyridine (99:1) as eluent to give the crude mixture. The crude mixture was further subjected to recycling GPC with toluene/pyridine (99:1) as eluent to separate the desired product **Ni-FP8** (0.11 mg, 11%). See Extended Data Fig. 1 for the reactions and Supplementary Information for characterisation data of intermediate compounds.

Substrate fabrication. The substrate used for **Ni-FP8** devices was fabricated using following procedure. On a degenerately *n*-doped silicon wafer with a layer (300 nm thick) of thermally-grown silicon dioxide (SiO_2), a local gate electrode (3 µm wide) was defined by optical lithography with lift-off resist and electron-beam (e-beam) evaporation of titanium (5 nm thick) and platinum (15 nm thick). A layer (10 nm) of hafnium dioxide (HfO_2) was then deposited by using atomic layer deposition (ALD). Next, source and drain contact electrodes separated by a 7 µm gap (the centre of the gap was aligned to the centre of the gate electrode, which means a 2 µm of horizontal distance between each electrode and gate electrode) were also defined by optical lithography with lift-off resist and electron-beam (e-beam) evaporation of titanium (5 nm thick) and platinum (45 nm thick). The procedure for the fabrication of substrates used for **Zn-P1** and **Zn-FP3** has published previously.

Graphene nanogaps. A layer (600 nm) of poly(methyl methacrylate) (PMMA) (with a molecular weight of 495 kDa) was spin coated onto chemical vapour deposition (CVD)-grown graphene (purchased from Grolltex) on copper. The copper was then etched in aqueous ammonium persulfate ((NH_4)$_2$$S_2$$O_8$) solution (3.6 g in 60 mL water) for 4 hours, after which the PMMA protected graphene was transferred 3 times to Milli-Q water and scooped up using the substrate. Air bubbles were further removed by partly submerging the sample in 2-propanol (IPA). The sample was dried overnight and baked at 180 °C for 1 h. The PMMA was then removed in hot acetone (50 °C) for 3 h.

The Z-shaped graphene tape with bow-tie shaped structure was patterned by e-beam lithography (EBL) with bi-layer lift-off resist (PMMA495 and PMMA950) and thermal evaporation of aluminium (50 nm thick). The *Z*-shaped

graphene pattern was used so the inner graphene leads are coplanar with the bowtie structure (see Fig. 1b, c), reducing tension on the bowtie-shaped graphene, and maximising the stability of the junction. PMMA e-beam resist was used as it is positive resist and it can be transformed into smaller molecules after exposure, which make it much easier to be completely removed than any negative photoresist. Aluminium was then deposited onto exposed area as oxygen plasma resist, as aluminium can be completely removed by either acidic or basic aqueous solutions. By this method we might avoid any contamination from residual photoresist on graphene. The flatter configuration and cleaner surface might provide stronger molecule-electrode coupling by better molecule-graphene interfacing. After lift-off, the graphene on unexposed areas (which are not covered by aluminium) was etched with oxygen plasma. The aluminium was subsequently removed by aqueous sodium hydroxide (NaOH) solution (0.5 M; 1.0 g in 50 mL water). The sample was finally immersed in hot acetone (50 °C) overnight to remove any residual PMMA. The optical image and SEM images can be found in Supplementary Information Section 1. The procedure for the fabrication of substrates used for **Zn-P1** and **Zn-FP3** has published previously.

Graphene nanogaps were prepared by feedback-controlled electroburning of the graphene bow-tie shape until the resistance of the tunnel junction is exceeded 1.3 GΩ (10^{-7} G_0), as shown in Fig. S1-5. The empty nanogaps were further characterised by measuring a current-map as a function of bias voltage (V_{sd}) and gate voltage (V_g) at room temperature in order to exclude devices containing residual graphene quantum dots[13], only clean devices were selected for further measurement.

Molecule junctions and measurements. The solutions of the porphyrin nanoribbon (1 μM in toluene) were drop-cast and allowed to dry in air. Only devices that showed clean current maps before molecule deposition were carried on further measurement. Thus, new signals appeared after molecule deposition can be safely attributed to transport through molecular junctions. Then, the chip contain molecular devices was connected to chip holder via wire bonding, loaded in Oxford Instruments 4K PuckTester, and cooled down to cryogenic temperature for detailed measurements. The current maps and differential conductance maps can be found in Supplementary Information Section 3.

Theoretical Calculations. Geometrical optimizations were carried out using the DFT code SIESTA[44], with a local density approximation LDA functional, a double-ζ polarised basis, a cut-off energy of 200 Ry and a 0.04 eV/Å force tolerance. From the Hamiltonian and overlap matrices of the DFT calculation of the junction, Gollum[45] calculates the transmission coefficient $T_{nm}(E)$ between scattering channels n, m in the electrodes, from which the transmission coefficient $T(E) = \sum_{nm} T_{nm}(E)$ is obtained. As discussed in chapter 17 of ref[46], this is equivalent to the expression:

$$T(E) = 4\mathrm{Tr}\left(\Gamma_1 G \Gamma_2 G^\dagger \right)$$

Where G is the (retarded) Green's function of the junction and Γ_i is the imaginary part of the self energy of electrode i. The electrical conductance is obtained from

$$G = G_0 \int_{-\infty}^{+\infty} T(E) \left(-\frac{\partial}{\partial E} f(E) \right) dE$$

where E_F is the Fermi energy of the device, $f(E) = \dfrac{1}{e^{(E-E_F)/k_B T} + 1}$ is the Fermi distribution function and $G_0 = \dfrac{2e^2}{h}$ is the conductance quantum. At low enough temperatures, this is approximated by $G = G_0 T(E_F)$. In

the presence of Cl atoms, spin polarised calculations were carried out to obtain the transmission coefficients $T^{\uparrow}$, $T^{\downarrow}$ for the two different spins, from which the total transmission coefficient $T = \dfrac{T^{\uparrow} + T^{\downarrow}}{2}$ is obtained.
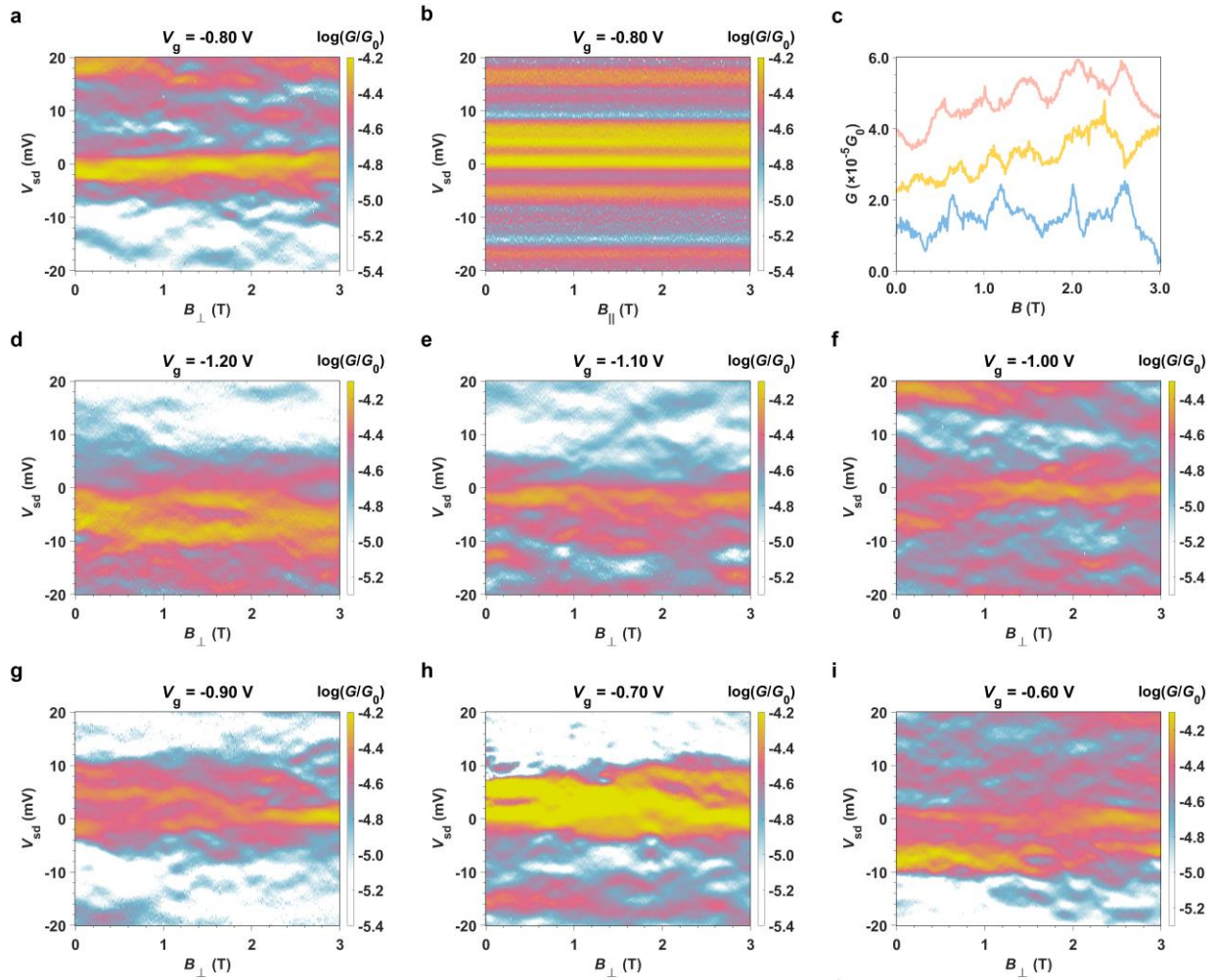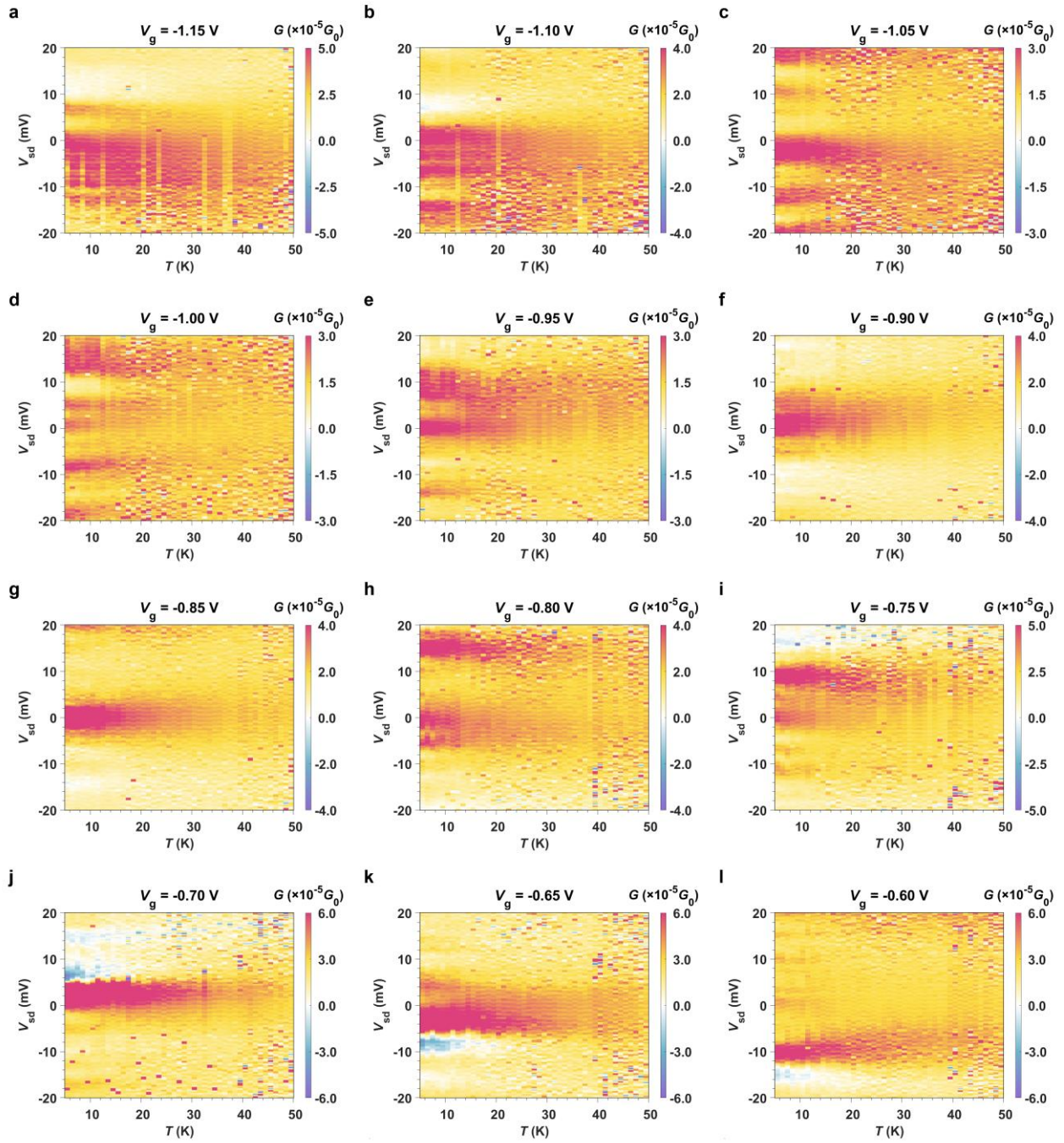
Extended Data
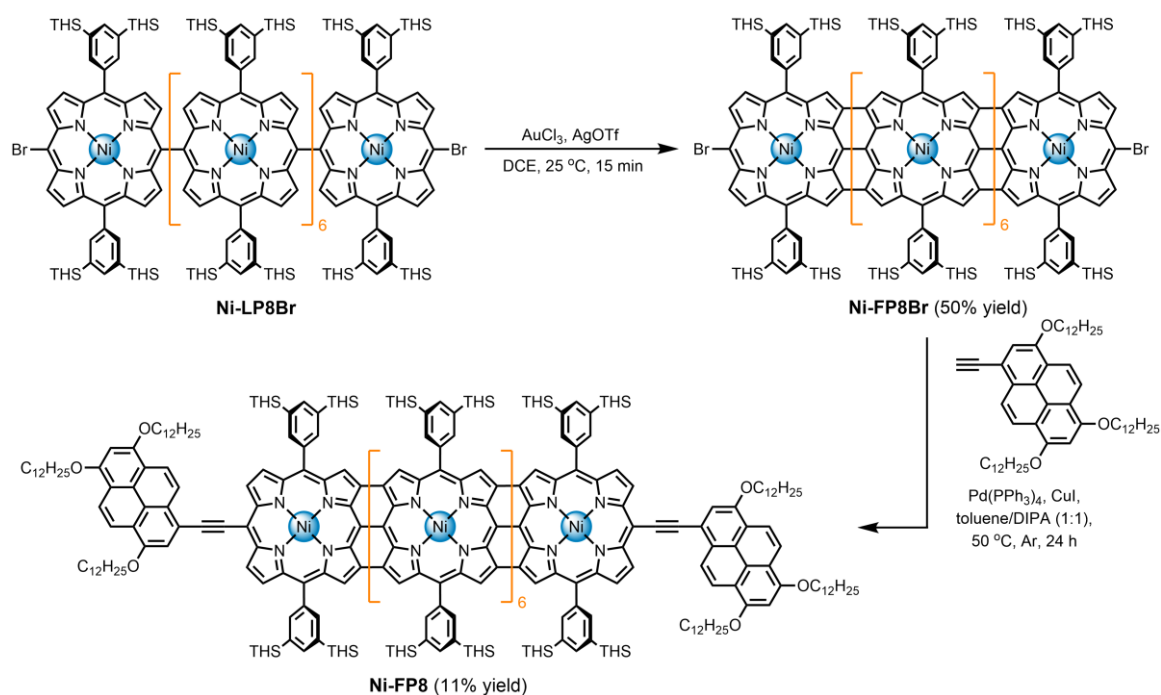
Extended Data Fig. 1 | Synthesis of fused porphyrin octamers Ni-FP8Br and Ni-FP8, THS = trihexylsilyl solubilising group.
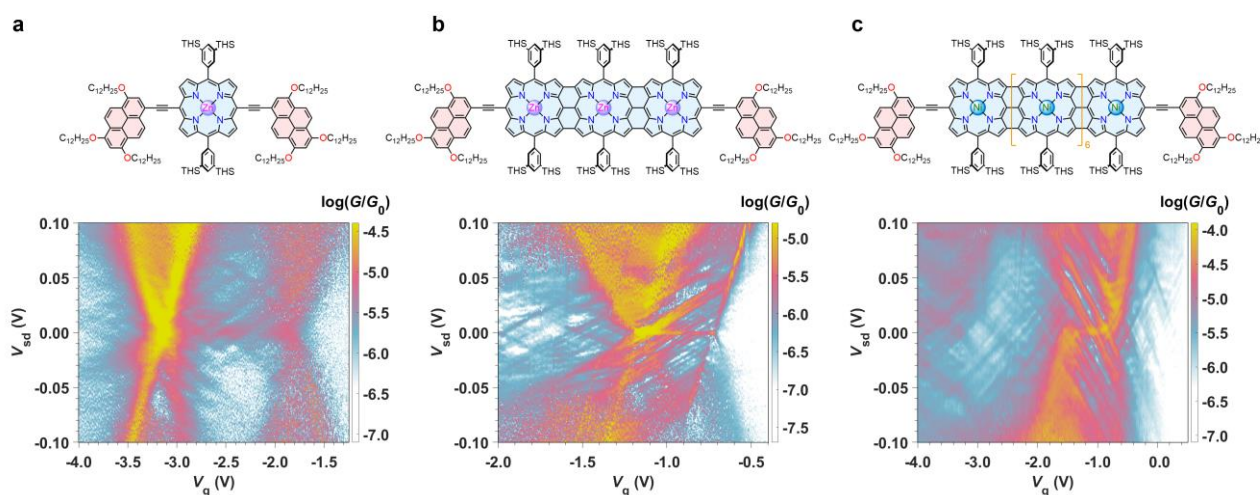
Extended Data Fig. 2 | Detailed differential conductance map of the region with interference pattern for zinc porphyrin monomer (a, Zn-P1), with edge-fused zinc porphyrin trimer (b, Zn-FP3) and edge-fused nickel porphyrin octamer (c, Ni-FP8).

Extended Data Fig. 3 | a, b Differential conductance map measured as a function of bias voltage (V_{sd}) and magnetic field (B) measured at a fixed gate voltage $V_g = -0.80$ V. The applied magnetic field is perpendicular ($\perp$, for **a**) and parallel ($\parallel$, for **b**) to transport plane (graphene), respectively. The interference pattern changes significantly as increasing perpendicular magnetic field, but unchanged in parallel magnetic field. **c** Weak magnetoconductance oscillations at $V_{sd} = -5$ mV (blue), 1 mV (yellow) and 9 mV (red) with a period of ~ 0.5 T (adjacent traces are offset for clarity), the origins of which are discussed in detail in the Supplementary Information. **d-i** Differential conductance map measured at different V_g under perpendicular ($\perp$) magnetic field. The oscillations on interference patterns are significant. Under parallel magnetic no obvious change was observed at all V_g, which are similar with that shown in **b** and not further shown here. Further details can be found in 'Magnetic field dependence' part in Supplementary Information Section 5.

Extended Data Fig. 4 | Differential conductance map measured as a function of bias voltage (V_{sd}) and temperature (T) measured at different V_g within the region with Kondo resonance.